Lawrence Berkeley National Laboratory

Title
Large polaron formation and its effect on electron transport in hybrid perovskites

Authors
Zheng, Fan
Wang, Lin-wang

Large Polaron Formation and its Effect on Electron Transport in Hybrid Perovskite

Fan Zheng and Lin-wang Wang*

Joint Center for Artificial Photosynthesis and Materials Sciences Division, Lawrence Berkeley National Laboratory, Berkeley, California 94720, USA.

E-mail: lwwang@lbl.gov

Abstract

Many experiments have indicated that large polaron may be formed in hybrid perovskite, and its existence is proposed to screen the carrier-carrier and carrier-defect scattering, thus contributing to the long lifetime for the carriers. However, detailed theoretical study of the large polaron and its effect on carrier transport at the atomic level is still lacking. In particular, how strong is the large polaron binding energy, how does its effect compare with the effect of dynamic disorder caused by the A-site molecular rotation, and how does the inorganic sublattice vibration impact the motion of the large polaron, all these questions are largely unanswered. In this work, using $CH_3NH_3PbI_3$ as an example, we implement tight-binding model fitted from the density-functional theory to describe the electron large polaron ground state and to understand the large polaron formation and transport at its strong-coupling limit. We find that the formation energy of the large polaron is around -12 meV for the case without dynamic disorder, and -55 meV by including dynamic disorder. By performing the explicit time-dependent wavefunction evolution of the polaron state, together with the rotations of $CH_3NH_3^+$ and vibrations of PbI_3^- sublattice, we studied the diffusion constant and mobility of the large polaron state driven by the dynamic disorder

1

and the sublattice vibration. Two effects of the inorganic sublattice vibration are found: on one hand, the vibration of the sublattice provides additional driving force for carrier mobility, on the other hand, the large polaron polarization further localizes the electron, reducing its mobility. Overall, the effect of the large polaron is to slow down the electron mobility by roughly a factor of two. We believe that both dynamic disorder due to rotation of the organic molecule, and large polaron effects induced by the polarization and vibration of the inorganic sublattice, play important roles for the electronic structure and carrier dynamics of the system.

Introduction. The outstanding performance of hybrid perovskites (HPs) as the solar cell has attracted a great number of studies to understand its fundamental physical principles. In addition to its high tolerence for defects,[1–4] the exceptionally long carrier lifetime and diffusion length despite the modest mobility for the excited carriers, have become the mostly focused research topic.[5–9] Many mechanisms have been proposed to explain such long carrier lifetime and diffusion length. For example, owing to the dipole moment of the molecules such as $CH_3NH_3^+$ (MA), it has been hypothesized that the polar nature of the molecule introduces the ferroelectricity and polar potential in HPs.[10] It has also been proposed that ferroelectric domain and domain walls contribute to the fast electron-hole separation and slow recombination.[11–14] Besides, the broken inversion symmetry can also lead to the so-called Rashba effect under the strong spin-orbit coupling introduced by heavy atoms such as Pb and I. The different spin chiralities and the momentum vectors of the band edge states with spin and momentum mismatch forbid the carrier-recombination in k space,[15–18] prolonging the lifetime of the excited carriers. However, the ferroelectricity of HPs has been under debate,[19,20] as many works show that this material could be centrosymmetric at room temperature owing to the fast reorientation of the molecules. In addition, pure inorganic halide perovskite $CsPbX_3$ also shows similar carrier behavior to the hybrid case.[21,22] Instead of forming ferroelectric domain, another explanation based on the dipole moment of the MA is the dynamic disorder, where the disordered orientation of the molecules exhibit random potential on inorganic sublattice such as PbI_3^-. Such variating potential modulates the band edge states of the electrons and holes, and produces spatially localized wavefunctions at different locations on a nano-size scale in real space,[23–26] which suppresses their recombination. Recently, more has been found that both the fast-rotating molecules and the soft inorganic sublattice can affect the carrier transport via the strong electron-phonon coupling.[15,27–29] Compared to conventional direct-band-gap semiconductors such as GaAs, the modest carrier mobility of $MAPbI_3$ indicates the contribution to the carrier scattering by optical phonon modes.[9,30,31] It is believed that with the relatively strong electron-phonon coupling, the large polaron can

3

be formed to develop the pseudo-free dressed carriers, and it can screen them from other carriers and defects to avoid recombination and trapping, which leads to long lifetime and long diffusion length.[32–36]

Large polaron refers to the shallow bound state due to Coulomb interaction between the charge carrier and the polarizable lattice. The so-called small polaron has been studied in this material, where the wavefunction is strongly localized within chemical bonds.[35–37] It is believed that the A-site molecules play a significant role in forming the small polarons, and such small polaron is crucial to explain the formation and annihilation of the trap states. However, different from the small polarons, large polaron often spreads over hundreds of unit cells owing to the relatively weak long-range Coulomb interaction and small lattice distortion by the longitudinal optical (LO) phonon mode.[38] It is suggested that the long time decay of more than 100 ps for the hot carrier relaxation in the experiments for various HPs,[7,39–41] could be owing to the large polaron screening[39,40,42] (at low excitation density) or the "phonon bottleneck" (at high excitation density caused by the large polaron overlapping).[27,43,44] The Fröhlich model further reveals the size of the large polaron and its transport estimated from model Hamiltonian.[27] Using the time-resolved optical Kerr effect spectroscopy, the large polaron formation time is estimated to be around 0.3ps to 0.7ps in MAPbBr$_3$ and CsPbBr$_3$.[45] A pioneer first-principle's calculation with hybrid exchange-correlation functional has shown the possible formations of large polarons in CsPbBr$_3$ and MAPbBr$_3$ along one direction, and has estimated their formation energies to be 140 and 60 meV, respectively.[46] In this calculation, it is observed that PbBr$_3^-$ lattice deforms under the charge of an electron or hole.[46] Due to the large computational cost, the first-principle calculation was only done for one dimensional polaron, instead of the real three dimensional case. Owing to the possibility of overestimation of wavefunction delocalization with LDA or GGA semi-local functional, direct density function theory (DFT) total energy calculation must be dealt with carefully to avoid self-interaction errors. Furthermore, the previous *ab initio* works only considered the static large polaron effect, without its coupling to the MA

4

molecular rotation, or sublattice vibration. As mentioned earlier, it has been experimentally confirmed that the MA molecules are randomly re-orientating in a sub-picosecond time scale. In our previous work,[24] we have shown that the random orientation of MA cause random potentials, which can localize the electrons and holes at different locations in real space and reduce their recombination. The rotation of MA also induces a dynamic disorder changing with time, providing a driving force for the carrier motion. Time-dependent Schrödinger's equation following the fluctuating potentials yields a carrier mobility, which agrees with the experimental value within its uncertainty range. However, in our previous work, the effects of the PbI_3^- inorganic sublattice has not been included. This sublattice has two additional potential effects, one is the large polaron bound polarization potential which further localizes the carrier wavefunction, another is the fluctuation of the lattice which provides additional driving force for the carrier movement.

In this work, we include the large polaron effect together with the dynamic disorder provided by the MA rotations and the vibrations of the PbI_3^- sublattice. Since the large polaron effect is caused by Coulomb interaction between the charge carrier and the lattice optical phonons, we construct a tight-binding (TB) model of MAPbI$_3$[15] following from DFT calculations. As shown previously,[24] such TB model can describe the carrier localization accurately, reproducing the large-scale DFT calculation results for tens of thousands of atoms. The formation of the polaron as well as its dynamics under the influence of the MA rotation and PbI_3^- sublattice vibration is simulated directly with a 48×48×48 supercell system with more than 1 million atoms. Our directly calculated formation energy agrees with the Fröhlich model within the strong coupling approximation. Since the temperature directly influences the rate of the molecular rotation, we compute the diffusion constant of the electron at different molecular re-orientation rates and with different PbI_3^- sublattice vibrations at different temperatures. The effect of PbI_3^- sublattice vibration is modeled with the molecular dynamics of the sublattice, which alters the TB model coupling parameters and on-site potentials. Our calculation suggests that the mobility of the electron is reduced

by a factor of 2 by including the polaron and sublattice vibrational effects. However, adding vibrational effect of the PbI_3^- sublattice tends to enhance the carrier diffusion more at high temperature than at low temperature. The resulting mobility are within the experimental uncertainty when compared with experimental values. By assuming a small activation energy for the molecular reorientation rate, we obtain the same trend of the mobility with respect to the temperature dependence as the experimental results.

Large Polaron Formation. A large polaron in a polarizable crystal is a result of two competing factors. On one hand, the localization of a carrier wavefunction causes a positive kinetic energy scaling as $1/L^2$ where L is the size of the localized state. On the other hand, such localized charge will induce the screening of the polarizable crystal lattice, resulting in a negative energy due to charge-polarization interaction scaling as $-1/L$. Note that it is important to avoid the erroneous self-interaction possibly exist in DFT total energy calculation which also scales as $1/L$. In DFT, the exact-exchange shall be used to cancel the self-interaction error originated from Coulomb energy. An incomplete cancellation (if using GGA or LDA) tends to yield a more extended polaron state. However, TB model used here does not have Coulomb interaction term, thus no self-interaction error. Without this self-interaction error, for sufficiently large L, the negative polarization energy will win and the total energy could be lowered compared to the delocalized Bloch state. Therefore, a large polaron can always be formed in a polarizable crystal, although its binding energy may be smaller than the room temperature thermal energy, making it hard to observe. The most popular large polaron Hamiltonian is proposed by Fröhlich, where the LO phonon model is assumed to couple to the electron wavefunction.[47] The exact Fröhlich model is difficult to solve due to correlation effect.[38] However, under the strong-coupling approximation, the large polaron wavefunction can be written as a product of the "electron" part and the "ionic" part under the Born-Oppenheimer (BO) approximation. Under this approximation, the total energy of the polaron is obtained by minimizing Eq.1 through variation of electron wavefunction ψ:

$$E = \langle \psi | H_0 | \psi \rangle - E^{\mathrm{P}}$$

$$E^{\mathrm{P}} = \frac{1}{2\bar{\epsilon}} \int d\mathbf{r} V^{\mathrm{P}}(\mathbf{r}) \rho(\mathbf{r}) \tag{1}$$

where H_0 is the Hamiltonian of the electron without polaron effect, $\rho(\mathbf{r}) = |\psi(\mathbf{r})|^2$ is the charge density for state $\psi(\mathbf{r})$, E^{P} indicates the screening energy, and V^{P} is the polarization potential of the lattice in response to the Coulomb potential of $\rho(\mathbf{r})$. The screening caused by electron-phonon coupling consisting of the ionic contribution of the dielectric constant is represented by $\bar{\epsilon}$: $\frac{1}{\bar{\epsilon}} = \frac{1}{\epsilon_\infty} - \frac{1}{\epsilon_0}$. ϵ_∞ and ϵ_0 are the electronic and static dielectric constants. Using DFT linear response theory,[48–53] we have calculated ϵ_∞ as 4.5, and ϵ_0 as 21. When the electron wavefunction is self-trapped in real space, it induces a distortion of the lattice to provide a polarization potential, which self-consistently localizes the electron wavefunction. Here, by expressing the electron energy with $\langle \psi | H_0 | \psi \rangle$, we avoid the self-interaction energy error. On the other hand, the screening of ψ due to other electron is represented by the ϵ_∞ in the expression of $\bar{\epsilon}$. By minimizing the total energy of Eq. 1 with respect to the wavefunction, we obtain the Hamiltonian:

$$H | \psi \rangle = \left(H_0 - \frac{1}{\bar{\epsilon}} V^{\mathrm{P}}[\rho] \right) | \psi \rangle = \epsilon | \psi \rangle \tag{2}$$

where V^{P} depends on the charge density ρ as $V^{\mathrm{P}}(\mathbf{r}) = \int d\mathbf{r}' \frac{\rho(\mathbf{r}')}{|\mathbf{r}-\mathbf{r}'|}$. To achieve self-consistency, an iterative scheme is used to solve the Hamiltonian by updating the wavefunction and polarization potential for every iteration. Since the electron charge density ρ is localized in a relatively large area (e.g. 50 Å), a macroscopic dielectric constant $\bar{\epsilon}$ can be used to describe its screening effect.

Due to the large size of large polarons, we use a supercell of 48×48×48 (corresponding to more than 300 Å lattice), which is large enough to model polaron and its transport.

7

154 Apparently, such large system is beyond the reach of DFT. Since we are only interested in
155 the conduction band edge for the electron, a tight-binding (TB) model with nearest-neighbor
156 hopping is used to construct a Hamiltonian (see Supplementary Information (SI)).[15] In this
157 TB model, the onsite energy and hopping magnitude are fitted to the DFT calculated band
158 structures. The TB parameters are listed in SI. These fitted parameters are also consistent
159 with the Hamiltonian obtained using the maximally-localized Wannier function represen-
160 tation.[54] Here, owing to its significance to the electronic structure,[16,55,56] the spin-orbit
161 coupling (SOC) is also included in the TB model[57] and the DFT calculations. As one can
162 see in Fig.S1 of SI, the TB model reproduces well the DFT band edge electronic structures.
163 Due to the sparse nature of the TB Hamiltonian, the parallelized ARPACK[58] math library
164 is used to solve the eigen states. The ARPACK packages also allows us to solve the interior
165 eigen states of the Hamiltonian. To solve Eq. 2 self-consistently, we start with a localized
166 wavefunction ψ (for example, with an Gaussian-shape initial potential), iterate through the
167 self-consistent equation until both kinetic energy ($\langle\psi| H_0 |\psi\rangle$) and potential energy ($E^{\mathrm{P}}$) are
168 converged.

169   Fig. 1a shows the charge density of the large polaron state and its polarization potential
170 $V^{\mathrm{P}}/\bar{\epsilon}$ (Fig. 1b) when we ignore the dynamic disorder potential due to the random orientation
171 of MA molecules. By comparing the energies with and without the large polaron effect, our
172 TB calculation reveals the formation energy of the large polarons in such a crystal is about
173 -12 meV. In Fröhlich model, a dimensionless coupling constant α is often used to quantify
174 the electron-phonon coupling strength:

$$\alpha = \frac{e^2}{\hbar} \frac{1}{4\pi\epsilon} \left(\frac{1}{\epsilon_\infty} - \frac{1}{\epsilon_0} \right) \sqrt{\frac{m^*}{2\hbar\omega_{\mathrm{LO}}}} \tag{3}$$

175 where ω_{LO} is the LO phonon frequency, and $m^* = 0.25$ is the effective mass of the electrons
176 (or $m^* = 0.55$ for holes), fitted from the DFT band structure. Particularly, our phonon cal-
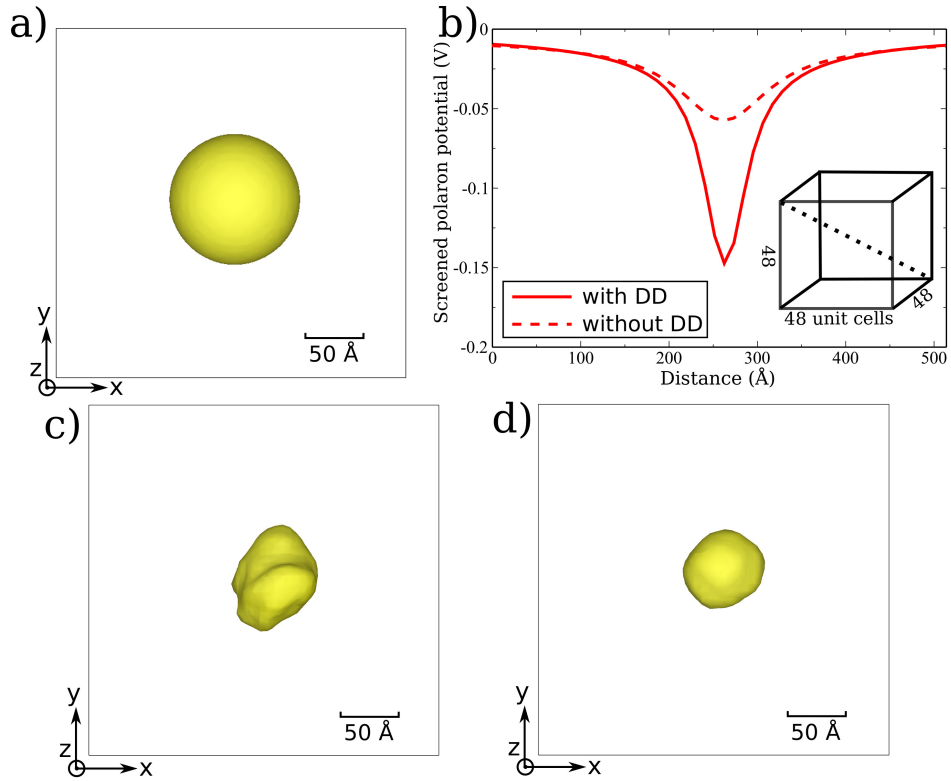
8

Figure 1: a) The conduction band minimum (CBM) state (charge density) with the large polaron effect (for clearness, all the atoms in this big supercell are not shown)
. b) The screened polaron polarization potential $V^{\mathrm{P}}/\bar{\epsilon}$ along the diagonal line of the cubic supercell (the diagonal line is shown in the inset diagram) for the case with and without dynamic disorder (DD) effect. c) The localized CBM state (charge density) induced by the DD without large polaron effect. d) The CBM state (charge density) under large polaron effect and DD. These states are plotted so that more than 85% charge is enclosed in the isosurface. The charge near the boundary of the supercell is negligible, showing that the size of the supercell is large enough.

9

culation and other work[59–61] show that there exist low energy LO phonons, corresponding to PbI$_3^-$ sublattice vibrations. We average the phonon frequencies weighed by their contribution to the low-frequency dielectric constant, and acquire ω_{LO} = 2.39 THz (SI). This value is consistent to both experimental[29] and theoretical[62,63] work. Using this phonon frequency, the α is estimated as 3.24, which is in line with other halide ionic crystals such as CsI (α=3.67), RbCl (α=3.81) or oxide perovskite SiTiO$_3$ (α=3.77).[64,65] The large α of MAPbI$_3$ falls in the low end region of the strong coupling. This picture is further supported by the recent experiment report the formation of strong-coupling polaron in HP.[66] Within the strong-coupling approximation, the polaron formation energy can be computed as $E = -0.106\alpha^2\hbar\omega_{LO} = -11$ meV,[47,67] which agrees well with our direct TB modeling result. Here, the specific value of ω_{LO} does not influence the Fröhlich calculated binding energy, since it has been canceled in the above formula and Eq. 3. Meanwhile, the polaron state (charge density) can be fitted to a Gaussian function. Thus, if defining the size of the polaron as the deviation of the Gaussian function ($\bar{r} \equiv \sigma$), the radius of the polaron states obtained from TB model is estimated to be 28Å. This is also consistent to 32Å computed based on the Fröhlich model at strong-coupling limit with the Gaussian approximation.[67]

As demonstrated in Ref. 24, the disordered MA molecular orientation produces potential variations on Pb and I atoms due to their dipole moments. Such random molecular potentials lead to the localized conduction band minimum (CBM) and valence band maximum (VBM) in the real space with nano-size scale as shown in Fig. 1c. This is a localized state before considering the large polaron effect, where the random potential is described inside H_0. By adding the large polaron effect as the second term in Eq.1, it further localizes the charge shown in Fig. 1d. A polaron size around 50 Å has been obtained. Compared to the large polaron without dynamic disorder (Fig. 1a), the charge density is much more localized. It is also more localized compared to the case of dynamic disorder without large polaron effect (Fig. 1c). The solid line in Fig. 1b indicates the converged polarization potential along the diagonal line of the super cell for the large polaron state under the dynamic disorder. The

10

maximum amplitude of this potential is 0.15 eV, which is similar to the dynamic disorder potential fluctuation which is around 0.2 eV as shown in Fig. S4.[24] However, this potential is more narrow compared with the dynamic disorder potential fluctuation. The additional large polaron binding energy is about -55 meV. This binding energy is much larger than the -12 meV binding energy in the case without dynamic disorder. This is because the dynamic disorder already pre-localizes the electron wavefunction. Using this polarization potential, the spatial displacements of ions in generating such polarization could be estimated based on their Born-effective charge (SI). We estimate that such displacement is in average on the order of 0.001 Å, which is smaller than the thermal fluctuations around 0.01~0.1 Å.

Polaron Transport. In our previous work,[24] it is suggested that the transport of the excited electron is mainly driven by the molecular rotation induced dynamic disorder. When a molecule changes its orientation, its electric static potential on the neighboring Pb and I atoms is altered. The aforementioned localized CBM state can "hop" to a new state once its energy crosses with the energy of another state. In this work, in order to model such dynamical process with large polaron effect (i.e. the polarization screening effect due to the PbI_3^- sublattice), the Monte-Carlo (MC) simulation of the MA rotation is performed with a rotation rate taken from experimental measurement. For each MC step, the total energy difference is computed by summing over the screened dipole-dipole interactions between the molecules. This energy difference is used to accept or reject trial rotations. In our model, molecular dipoles are interacting with each other via the screened dipole-dipole interaction with the screening coming from the inorganic PbI_3^- sublattice. The total energy by summing over dipole $\mathbf{d}$ at site-m is expressed as:

$$E_{\text{tot}} = \sum_m \mathbf{d}_m \cdot \tilde{\mathbf{E}}_m$$

$$\tilde{\mathbf{E}}_m = \frac{1}{\epsilon_n} \sum_n \mathbf{E}_m(n) + \frac{1}{\epsilon_{n'}} \sum_{n'} \mathbf{E}_m(n') + \frac{1}{\epsilon_{n''}} \sum_{n''} \mathbf{E}_m(n'') + \frac{1}{\epsilon_{n'''}} \sum_{n'''} \mathbf{E}_m(n''') \tag{4}$$

11

where $\tilde{\mathbf{E}}_m$ is the screened electric field from other dipoles applied to the dipole at site m.

Here, we believe that dipoles at different distances will have different screening effect from

the PbI_3^- sublattice in order to mimic the reciprocal-vector dependent screening. Therefore,

we partition the spatial summation into four different layers (n: nearest neighbor; n': next-

nearest neighbor; n'': third-nearest neighbor; n''': others) with different dielectric constants.

$\epsilon_{n'''}$ is known as 21, corresponding to the low frequency dielectric constant ϵ_0. Besides

electric field, the average potential at MA molecule sites ($V_m = \frac{1}{\epsilon_n} \sum_n V_m(n) + \frac{1}{\epsilon'_n} \sum_{n'} V_m(n') +$

$\frac{1}{\epsilon''_n} \sum_{n''} V_m(n'') + \frac{1}{\epsilon'''_n} \sum_{n'''} V_m(n''')$) is screened with the same set of dielectric constants. The

dielectric constants (ϵ_n, $\epsilon_{n'}$, and $\epsilon_{n''}$) are obtained by fitting the *potentials* computed from the

above screened dipole-dipole model to the averaged potentials of a molecule extracted from

DFT calculations (SI) with many random configurations of the MA molecules. For a given

MA orientation configuration, the PbI_3^- sublattice is fully relaxed. Thus, the DFT potential

contains the screening effect of the PbI_3^- sublattice, as described in Eq. 4. Fig. 2 shows the

comparison of the potential obtained between the above model and DFT potential, which

demonstrates the validity of our screening model.

After each MC step, their potentials on each Pb and I atoms are re-evaluated. Between

two MC steps, the potential change is interpolated linearly into small time steps (~0.048fs)

in order to carry out the evolution of the wavefunction. The time-dependent wavefunction

evolution are solved following the Schrodinger's equation by applying the evolution operator

to the wavefunction directly:

$$\begin{aligned}
\psi(t+dt) &= e^{-iH(t)dt}\psi(t) \\
&\approx \left[1 - iH(t)dt - \frac{1}{2}H^2(t)dt^2 + \frac{i}{6}H^3(t)dt^3 + \frac{1}{24}H^4(t)dt^4 \right]\psi(t)
\end{aligned} \quad (5)$$

The evolution operator is expanded up to the forth order of dt to ensure the convergence of

the evolution regarding to dt. Here, H is defined in Eq. 2.

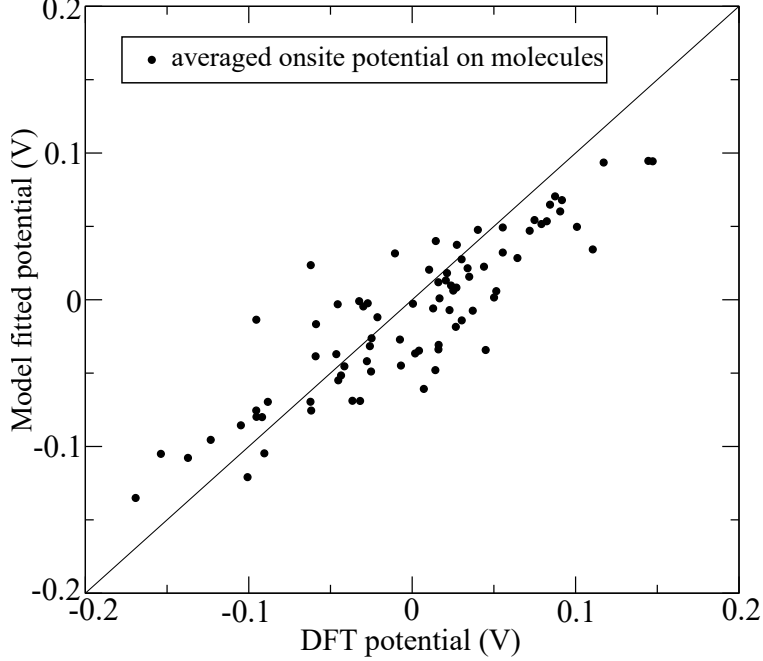Figure 2: The comparison between the potentials calculated from DFT and the fitted layer-dependent dipole-dipole screening potential.

With the setup of Eq. 5, now we can consider the effects of the large polaron. Two effects are associated with the PbI_3^- sublattice. The first is the change of polarization following the change of charge density $\rho(\mathbf{r})$, the second is the thermal fluctuation of the PbI_3^- sublattice. We first consider the polarization change. The PbI_3^- sublattice polarization will follow the movement of $\rho(\mathbf{r}) = |\psi(\mathbf{r})|^2$. However, such polarization by lattice distortion is not instantaneous, instead, some sub-piecosecond is needed to form a large polaron as discussed before. Thus, when the electron hops from one location to a new location, the change of the lattice screening owing to the new charge density shall also be retarded. To represent this effect, we mix the old polarization potential and the new potential with a ratio weighted by the evolution time and the polaron formation time as:

$$V^{\mathrm{P}}_{t_{n+1}} = V^{\mathrm{Poisson}}_{t_{n+1}}[\rho_{t_{n+1}}]\left(1 - e^{-\frac{dt}{\tau}}\right) + V^{\mathrm{P}}_{t_n}e^{-\frac{dt}{\tau}} \tag{6}$$

where V^{Poisson} is the instantaneous polarization potential calculated from Poisson solver with

13

259 charge density $\rho_{t_{n+1}}$, τ is the large polaron formation/annihilation time, and $dt = t_{n+1} - t_n$.

260 The resulting $V_{t_{n+1}}^{P}$ is used for the second term in H of Eq. 2. In the experiment, the polaron

261 formation time has been estimated to be around 0.3 and 0.7 ps for MAPbBr$_3$ and CsPbBr$_3$

262 respectively. There is no estimation of τ for MAPbI$_3$. In our simulation, we have tested

263 τ = 0 fs, 80 fs, 150 fs and 300 fs, and large τ only slightly reduce the diffusion constant

264 (SI). However, the reduction is quite small compared to other factors discussed below. Thus,

265 we have used τ = 80 fs for our calculations. Such retarded potential is then added to the

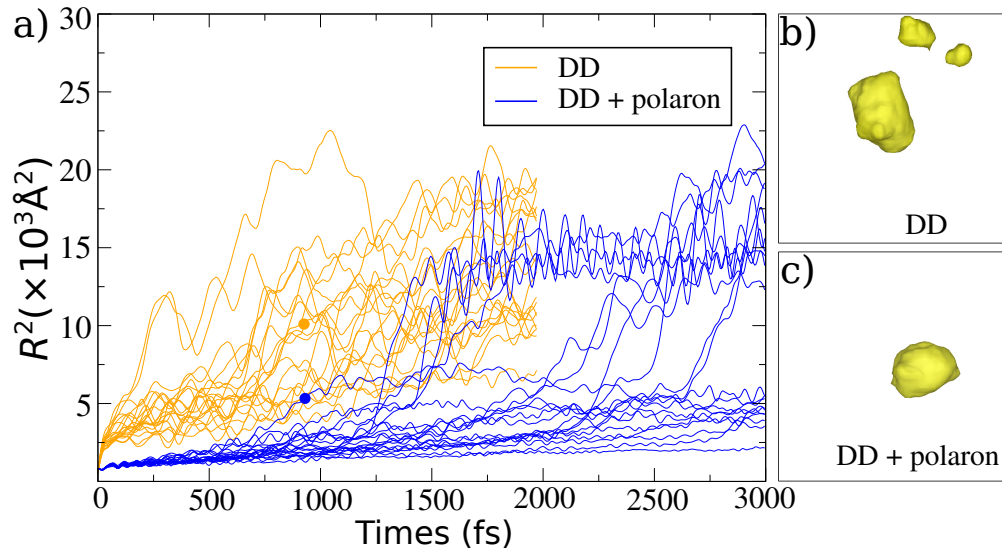266 Hamiltonian and the wavefunction evolution.

Figure 3: a) $R^2(t)$ of 20 independent trajectories for the case (orange line) with dynamic disorder only (DD) and the case (blue line) with both dynamic disorder and large polaron. The molecular rotation time used in this graph is 6 ps. b) Snapshot of the wavefunction (charge density) for the case with dynamic disorder only at time t = 900 fs. This state is picked up from the trajectory with orange dot in a). c) Snapshot of the wavefunction (charge density) for the case with dynamic disorder and large polaron effect at time t = 900 fs. This state is picked up from the trajectory with blue dot in a).

267 With this in place, now we can study the effects of polaron on the carrier diffusion. In our

268 dynamical simulation, the time step dt for the wavefunction evolution is 2 a.u. (around 0.048

269 fs) to ensure its stability. For every ten dt steps, a MC step is applied to rotate the molecules.

270 To capture the change of the polaron polarization potential, the Poisson equation is re-solved

271 based on the charge density for every 5 fs. To quantify the diffusion process, $R^2(t)$ has been

14

calculated as shown by Fig. 3a, where $R^2(t) = \langle \psi(t) | (\mathbf{r} - \mathbf{r}_0)^2 | \psi(t) \rangle$ is evaluated for the localized wavefunctions. $\mathbf{r}_0$ is the center of mass of the charge density at $t = 0$. The initial wavefunction square $|\psi|^2 (t = 0)$ is shown as Fig. 1d. To illustrate the wavefunction evolution, we show the states at $t = 900$ fs for a given trajectory shown in Fig.3a with and without the large polaron effect in Fig. 3b and c, respectively. We can see that the originally localized CBM state in the center of the box starts to diffuse off center in the case with dynamic disorder and large polaron. For the case with dynamic disorder only, the wavefunction has been broken down into a few pieces. In order to further quantify the diffusion of the large polaron, we perform 20 independent trajectories starting from the same initial state with different random MC seeds, with and without the large polaron effect. The $R^2(t)$ of all the 20 trajectories are shown in Fig. 3a. For the case without polaron, the carrier can quickly escape from the center after 200 fs from the initial state. Moreover, once the carrier is hopped away, its R^2 value oscillates strongly, indicating a strong spatial variation of the wavefunction in real space. However, by including polaron effect, some of the trajectories have very small increments even after a long time. This corresponds to the situation that these localized states are still in the center and do not get a chance to hop. In general, the carrier needs to spend more than 1ps before it can accumulate enough potential variations in order to overcome the initial polarization potential and hop to a different place. Once the carrier is moved, it tends to stay in a new place for a while before jumping to another location, showing a step-like R^2. But the important conclusion is that the polarization potential does not completely trap the carrier in a location permanently. The carrier can still move and hop to a new place, albeit such hopping rate is smaller than the case without the large polaron effect. By averaging $R^2(t)$ for all the trajectories, we compute the diffusion coefficient D as $\bar{R}^2(t) = \langle R^2(t) \rangle = 6Dt$.[24] The averaged $R^2(t)$ forms a straight line as we expected (Fig. 4a), and the slope of this straight line yields the diffusion constant D. By doing so for each rotation rate, we obtain Fig. 4b, where the diffusion constants are compared for the case with dynamic disorder only and case with dynamic disorder and large polaron polarization

299 (but without yet the thermal fluctuation of the PbI$_3^-$ sublattice). The diffusion constants

300 without the large polaron effect agree with our previous results in Ref. 24, although some

301 modifications have been made both for the TB model and the screening model of Eq. 4. The

302 large polaron reduces the diffusion coefficient by a factor of 2. This is because the additional

303 polaron polarization potential further localizes wavefunction and deepens the localization

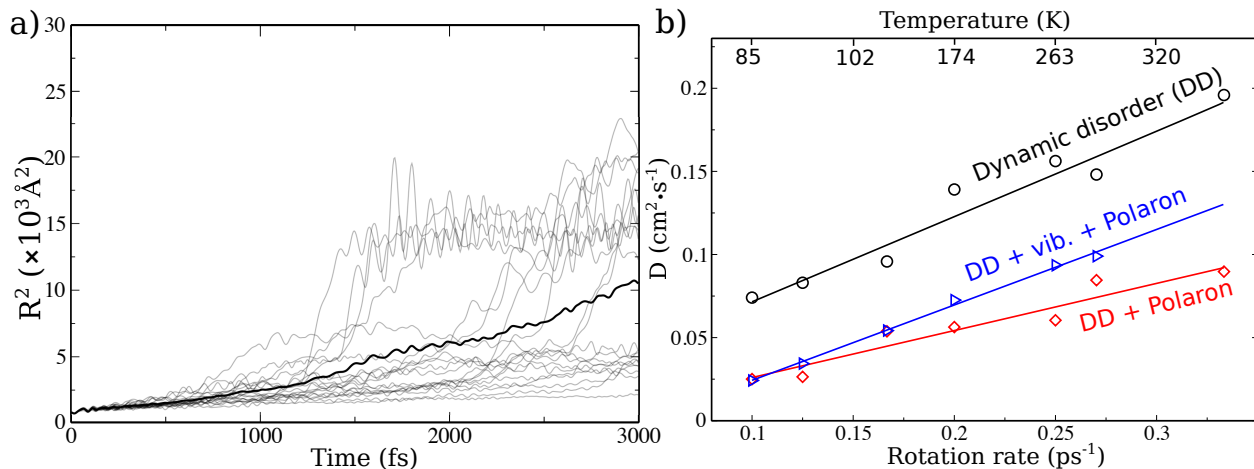304 potential, thus makes the hopping more difficult.

Figure 4: a) The $R^2(t)$ evolution along time for 20 independent trajectories (grey lines) under rotation time at 6 ps. The thick black line indicate the averaged value of the 20 trajectories $\bar{R}^2(t)$. b) The diffusion constant D obtained for different rotation rates for the three cases: dynamic disorder (DD) only, DD + large polaron, DD + PbI$_3^-$ sublattice vibration + large polaron. The temperature T used in the lattice vibration and MC simulation of DD is correlated with the rotation rate as: rate $\propto e^{-(10\text{meV}/kT)}$.[24]

305 Up to now, we have discussed the effects of the large polaron and A-site molecular

306 orientation flipping induced dynamic disorder to the carrier dynamics. Besides forming the

307 polarization potential in response to the carrier charge density, the thermal vibrations of

308 PbI$_3^-$ sublattice can also exert a driving force to induce the carrier motion in addition to the

309 dynamic disorder potential fluctuation. Such thermal vibrational effect can be represented

310 by the variation of Pb and I onsite potentials and the change of the TB coupling strength

311 between two neighboring Pb and I atoms. Unfortunately, there is no easy realistic calculation

312 to capture both effects at the same time. Instead, we have used a model dynamics to describe

313 the onsite energy fluctuation, and a classical MD to simulate structural distortion which

16

³¹⁴ results in the change of TB coupling strength. Note that here, the Pb and I onsite potential

³¹⁵ fluctuation refers to the fluctuation caused by the thermal movement of Pb and I atoms, not

³¹⁶ the fluctuation caused by the MA molecular rotations, which has been already included in

³¹⁷ the dynamic disorder model. This statistic feature of the onsite potential fluctuation can be

³¹⁸ collected from a small supercell *ab initio* MD while fixing the MA molecules. Fig. 5 shows the

³¹⁹ averaged Pb-, I- onsite auto-correlation function and nearest neighboring Pb–I pair potential

³²⁰ correlation functions, obtained from a DFT trajectory (SI) with fixed MA molecules. The

³²¹ relatively simple oscillations of the DFT onsite potential auto-correlation functions allow us

³²² to fit it with an onsite Langevin dynamics model comprising of simple oscillators. In this

³²³ model dynamics, the equation of motion for one Pb or I is expressed as $\ddot{x} = -c\dot{x} - kx + F_{\text{random}}$,

³²⁴ x is the variable to describe the dynamics of the potential, parameters c and k control

³²⁵ the damping rate and oscillation frequency respectively, and F_{random} is the random force

³²⁶ applied to each Langevin step. These dynamic models are carried out independently for

³²⁷ each atom with different parameters for Pb and I sites, denoting their results as $x_i^{\text{Pb}}(t)$ and

³²⁸ $x_i^{\text{I}}(t)$, and i indicates the lattice site. To yield the correct nearest-neighbor Pb–I correlation

³²⁹ function, we also mix the dynamics of neighboring Pb and I as following: $V_i^{\text{Pb}}(t) = \alpha_1 x_i^{\text{Pb}}(t) +$

³³⁰ $\beta_1 \sum_{\text{neigh}} x_j^{\text{I}}(t)$, $V_i^{\text{I}}(t) = \alpha_2 x_i^{\text{I}}(t) + \beta_2 \sum_{\text{neigh}} x_j^{\text{Pb}}(t)$, here $V_i^{\text{Pb}}(t)$ and $V_i^{\text{I}}(t)$ are the final Pb and

³³¹ I onsite potential to be added in H_0 with α and β as fitting parameters. All the parameters

³³² used in the model and the mixing weights are tuned so that both the onsite auto-correlation

³³³ function and neighboring-pair correlation functions of $V_i^{\text{Pb}}(t)$ and $V_i^{\text{I}}(t)$ match DFT as

³³⁴ shown in Fig. 5. Using this model dynamics, the full onsite potential time evolution profiles

³³⁵ of all the Pb and I atoms in the 48×48×48 supercell can be obtained. Meanwhile, in order

³³⁶ to simulate the PbI_3^- sublattice vibration thus its effects on TB coupling, we performed

³³⁷ the classical MD with LAMMPS[68] using force field designed for MAPbI$_3$ for the 48×48×48

³³⁸ supercell at different temperatures [69] (SI). Our tight-binding model is capable to evaluate

³³⁹ the change of the hopping strength based on the Pb–I bond-length deviation with the general

³⁴⁰ form $h = h_0 e^{-\lambda(b-b_0)}$, where h_0 and b_0 are the equilibrium hopping strength and bond length,

17

respectively. Here, λ of different bond types are given from Ref. 70, where they are fitted by the Wannierization of large number of structures with different bond distortions.
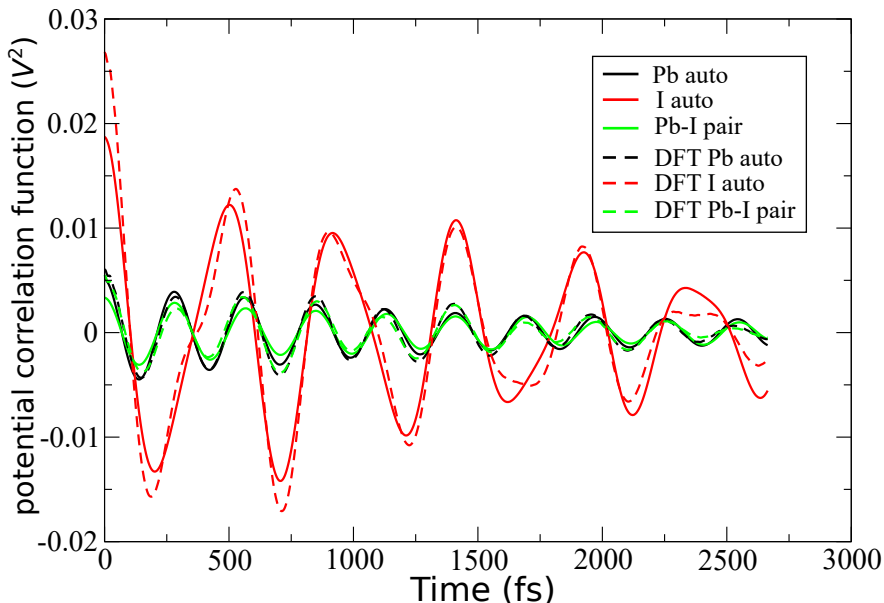

Figure 5: a) The Pb autocorrelation, I autocorrelation, neighboring Pb–I pair correlation functions computed from Langevin model dynamics and DFT *ab initio* MD.

With the onsite potential and the local TB coupling parameter time evolution profiles for the 48×48×48 supercell, the PbI_3^- sublattice thermal vibration effect is added to the time-evolution of the wavefunctions described by Eq. 5. All these effects are included in H_0 of Eq. 2. Owing to the relatively slow change of the onsite potential and bond length by phonons, we update the PbI_3^- structure and the corresponding parameters for every 5 fs. During the 5 fs, the onsite energies and the hoppings are interpolated linearly to small dt to evolve the wavefunction. To investigate the sublattice vibrational effects at different temperatures, we have calculated the diffusion constants at different temperatures including the effects of dynamic disorder, large polaron and sublattice vibration as shown in Fig. 4. In Fig. 4,we have used the MA molecular rotation rate as the horizontal axis while using a rate $\gamma \propto e^{-E_a/kT}$ by assuming the MA rotation activation energy E_a = 10 meV to correlate between different MA rotation rate and temperature T.[24] Intuitively, the sublattice vibration should enhance the carrier diffusion for all the temperatures, because the onsite potential

variation and TB coupling strength change tend to offer additional random driving force for the carrier movement in addition to the dynamic disorder caused by molecular re-orientation. However, our simulation shows such effect is not homogeneous at different rotation rates. At high rotation rate (also high temperature), the enhancement of carrier mobility is obvious. While, at the low rotation rate (low temperature), the increase is less pronounced. We think this is because there are actually two possible effects of the PbI_3^- sublattice vibration, similar to the that of the MA molecule re-orientation. The fluctuation caused by PbI_3^- sublattice vibration can also further localize the carrier, in addition to providing the movement driving force. Such enhanced localization introduces deeper polaron polarization potential, and tend to slow down the carrier motion. This is illustrated in Fig. S6, where the lowest polaron potentials are extracted. By rotating exactly same molecular dipoles every MC step for the two cases with and without PbI_3^- sublattice vibrational effect, the polarization potential difference is purely caused by the sublattice vibrations, and such effect deepens the polarization potential. It seems that the two effects of PbI_3^- vibration are competing with each other. Perhaps at higher temperature, the driving force effect dominates, hence it increases the carrier diffusion, while in lower temperature, there two effects cancel out each other.

After the diffusion constant is obtained, the mobility can be evaluated by $\mu = D/k_{\rm B}T$. However, the carrier mobilities vary widely from different experiments[30] (Fig.6). Even for the mobilities measured with the same method, their values could be quite different. Therefore, it is very difficult to compare with the experiments directly. Our calculated mobility is found to be close to the experimental value. By adding the polaron effect, the mobility of the carriers is reduced by half. However, the effect of the PbI_3^- sublattice vibration tends to shift up the mobility, into the range of 3 to 5 cm^{2}V^{-1}s^{-1} at the molecular rotation rate between 3ps to 10ps. Overall, our results agree with the experiments as we have shown for comparison,[71,72] especially for the trend. If we fit the temperature-mobility dependence to the relation $\mu \propto T^k$ for full temperature range, k=-0.523 (DD), -0.448 (DD+Polaron),
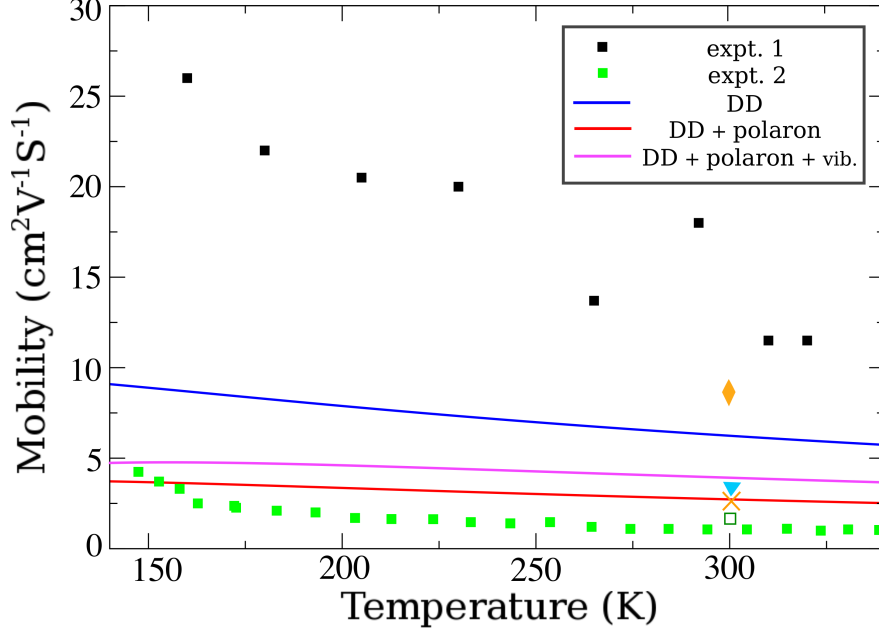
19

Figure 6: The calculated mobility with respect to the temperature considering different effects: dynamic disorder (DD) only, DD+large polaron, DD+large polaron+PbI_3^- phonon. The experimental values are from Ref. 71 for expt. 1 and Ref. 72 for expt. 2. Other experimental measured mobilities are also listed, ×: Ref. 73 (μ_e), ▼: Ref. 74 (μ_e), □: Ref. 75 ($\mu_e + \mu_h$), ◆: Ref. 76 ($\mu_e + \mu_h$).

and -0.318 (DD+Polaron+vib) are obtained. Similar to the measured mobilities, values of k could be quite different. Many experiments have yielded $k \approx$-1.5[71,72,77,78] fitted for tetragonal phase only or together with orthogonal phases, but other values k=-2.8(e^-) and -2.0(h^+) are also obtained.[79] However, the dynamic disorder effect caused by the molecules becomes more prominent at high temperature. At low temperature, the rotation of the molecules is further constrained by the PbI_3 sublattice, and their orientation becomes more ordered,[80] which may suppress the carrier localization. Meanwhile, ϵ_0 could have strong temperature dependence at low temperature, which alters polaron polarization screening. Therefore, if we fit k only in high temperature range (for example >290K), we obtain k=-0.65 (DD), -0.63 (DD+Polaron), and -0.55 (DD+Polaron+vib). This result is in line with k=-0.42, fitted from the measured mobilities of experiment 2[72] at high temperature range (>290K). Recent theoretical work[62] also achieve k value around -0.46, consistent to what we get. Considering the differences of experiment 1 and 2, in experiment 1,[71] they used PL and THz conductivity spectra to

study the temperature dependent mobility. In experiment 2,[72] the time-resolved microwave conductivity technique was used to explore effect of A-site cation to the carrier dynamics. The reason for the large difference between the two experiments could be complicated, it might depend on the sample condition due to different synthesize conditions etc. If we assume the sample conditions are the same, then the better agreement with experiment 2 could be because the electric field used in microwave probe is weak,[72] which is consistent with the weak field limit in our calculation. The strong electric field in THz measurement may introduce non-linear mobility effect, as the potential drop caused by each hopping is in the same order as the potential barrier for the wavefunction localization. Furthermore, the THz frequency time is similar to the phonon frequency, which in some degree might freeze the lattice polarization in its measurement. As a result, its measured mobility might be more close to our previous study without large polaron effects, as shown in Fig.6. In our current simulation, the A-site is occupied by the polar molecules. For pure inorganic halide perovskite such as $CsPbX_3$, the displacement of Cs^+ atom will contribute to the formation of the large polarons. However, without the slow rotational degree of freedom of the A-site molecule, the large polaron may be hard to form, and it will have a much smaller binding energy. This may explain the higher mobility observed in $CsPbBr_3$.[26,72,81] In this work, the large polaron of the hole is not discussed. However, as shown in our previous work,[23] the electron and hole are localized at different locations due to the potential fluctuation caused by the random orientation of the MA molecule. Large polaron tends to further localize them, thus their reduced spatial overlap may lower the radiative recombination and enhance the lifetime.

In the end, we want to justify the hopping picture and the BO approximation we have used throughout this work. There have been continuous efforts to understand the large polaron in hybrid perovskites, e.g. using Bloch state as the starting point to include the scattering of optical phonon modes.[31] For a conventional perfect crystal structure such as GaAs with weak electron-phonon coupling, the Boltzmann equation is more appropriate to describe the large

21

polaron transport with the Bloch state as a starting point,[82] although there are also attempts to use hopping picture for large polaron transport even in perfect crystal,[83] However, hybrid perovskite including $MAPbI_3$ is not a usual "perfect crystal". Recent experiments and theoretical work have shown the strong electron-phonon coupling and indicated that the carrier could be localized under the random orientation of A-site molecules, which is also why these materials are unusual and fascinating. Under this circumstance, the charge is already localized before any additional large polaron induced localization. Thus, the hopping picture of such localized charge is more appropriate to study its transport. This is different from the hopping picture used for small polarons, where the localized states hops between nearby bonds within a unit cell. In this work, the hopping distance is typically comparable to the localization size, thus much larger than the nearest neighbor atomic distance. As for the BO approximation, when electron-phonon coupling is small (weak-coupling limit, such as GaAs), the phonon affects the electronic structure in a perturbed way. The electron and phonon are correlated dynamically, and the BO approximation is unsuitable. However, when electron-phonon interaction is strong (strong-coupling limit), the phonon cannot respond to the fast electron movement to necessitate the correlated perturbation treatment. Therefore, the adiabatic BO approximation can be used, as discussed in this work. Another important reason for the BO approximation is that, as discussed above, the wavefunciton is already localized under dynamic disorder before any polaron effect, which will significantly reduce the correlation effect. As we show in our paper, the polaron binding energy for a localized electron becomes much larger. Under our adiabatic approximation, these two localizations (caused by large polaron and dynamic disorder) are treated on equal footing, there is no approximation between them (not treating one as an perturbation to another). Of course, the perfect method to solve the large polaron at any coupling is to use Feynman's path integral. But this is still hard to apply to a realistic system at the atomic level.

Summary. In summary, by using the tight-binding model fitted to the first-principles DFT calculations, we studied the large polaron formation and its effects on carrier transport

22

in MAPbI$_3$. We provide an atomic and quantitative picture to understand the large polaron effect in MAPbI$_3$. We studied two effects of the PbI$_3^-$ sublattice to the carrier mobility. The first is the large polaron polarization effect, which tends to further localize the carrier wavefunction on top of the dynamic disorder caused by MA molecule rotation. The second is the thermal vibration of the PbI$_3^-$ sublattice which provides randomness to further localize the wavefunction, but also a driving force for carrier movement. Our calculation shows a large polaron with formation energy around 12 meV for one electron carrier when there is no molecular disorder, which is consistent with the Fröhlich model at strong coupling limit. By adding dynamic disorder, the large polaron binding energy is increased to 55 meV. This polaron state is accomplished by a lattice polarization potential around 0.14 eV, only slightly smaller than the 0.2 eV potential fluctuation caused by the MA molecular random orientation. By solving the time-dependent Schrodinger's equation and performing MC simulation, we study how the electron state evolves under the driving force of the molecular re-orientation and the lattice vibration. We find that the polaron effect slows down the mobility of the electrons by a factor of 2. On the other hand, the PbI$_3^-$ sublattice vibration enhances the electron mobility particularly at high temperature. Overall, the computed mobility is in line with the experimental measurements. Our calculation reveals how the large polaron state is formed and its role in carrier movement in the MAPbI$_3$ system.

Acknowledgement

the discussions and his help to the classical MD simulation.

References

(1) Buin, A.; Pietsch, P.; Xu, J.; Voznyy, O.; Ip, A. H.; Comin, R.; Sargent, E. H. Materials Processing Routes to Trap-Free Halide Perovskites. *Nano Letters* **2014**, *14*, 6281–6286.

(2) Kim, J.; Lee, S.-H.; Lee, J. H.; Hong, K.-H. The Role of Intrinsic Defects in Methylammonium Lead Iodide Perovskite. *The Journal of Physical Chemistry Letters* **2014**, *5*, 1312–1317.

(3) Kang, J.; Wang, L.-W. High Defect Tolerance in Lead Halide Perovskite CsPbBr3. *The Journal of Physical Chemistry Letters* **2017**, *8*, 489–493.

(4) Yin, W.-J.; Shi, T.; Yan, Y. Unusual Defect Physics in CH3NH3PbI3 Perovskite Solar Cell Absorber. *Applied Physics Letters* **2014**, *104*, 063903.

(5) Brenner, T. M.; Egger, D. A.; Kronik, L.; Hodes, G.; Cahen, D. Hybrid Organic—inorganic Perovskites: Low-Cost Semiconductors with Intriguing Charge-Transport Properties. *Nature Reviews Materials* **2016**, *1*, 15007.

(6) Stranks, S. D.; Eperon, G. E.; Grancini, G.; Menelaou, C.; Alcocer, M. J. P.; Leijtens, T.; Herz, L. M.; Petrozza, A.; Snaith, H. J. Electron-Hole Diffusion Lengths Exceeding 1 Micrometer in an Organometal Trihalide Perovskite Absorber. *Science* **2013**, *342*, 341–344.

(7) Zhu, H.; Miyata, K.; Fu, Y.; Wang, J.; Joshi, P. P.; Niesner, D.; Williams, K. W.; Jin, S.; Zhu, X.-Y. Screening in Crystalline Liquids Protects Energetic Carriers in Hybrid Perovskites. *Science* **2016**, *353*, 1409–1413.

(8) Dong, Q.; Fang, Y.; Shao, Y.; Mulligan, P.; Qiu, J.; Cao, L.; Huang, J. Electron-

Hole Diffusion Lengths > 175 Mm in Solution-Grown CH3NH3PbI3 Single Crystals. *Science* **2015**, *347*, 967–970.

(9) Brenner, T. M.; Egger, D. A.; Rappe, A. M.; Kronik, L.; Hodes, G.; Cahen, D. Are Mobilities in Hybrid Organic–Inorganic Halide Perovskites Actually "High"? *The Journal of Physical Chemistry Letters* **2015**, *6*, 4754–4757.

(10) Frost, J. M.; Butler, K. T.; Brivio, F.; Hendon, C. H.; van Schilfgaarde, M.; Walsh, A. Atomistic Origins of High-Performance in Hybrid Halide Perovskite Solar Cells. *Nano Letters* **2014**, *14*, 2584–2590.

(11) Liu, S.; Zheng, F.; Koocher, N. Z.; Takenaka, H.; Wang, F.; Rappe, A. M. Ferroelectric Domain Wall Induced Band Gap Reduction and Charge Separation in Organometal Halide Perovskites. *The Journal of Physical Chemistry Letters* **2015**, *6*, 693–699.

(12) Rashkeev, S. N.; El-Mellouhi, F.; Kais, S.; Alharbi, F. H. Domain Walls Conductivity in Hybrid Organometallic Perovskites and Their Essential Role in $CH_3NH_3PbI_3$ Solar Cell High Performance. *Scientific Reports* **2015**, *5*, 11467.

(13) Chen, Y.-F.; Tsai, Y.-T.; Bassani, D. M.; Hirsch, L. Experimental Evidence of the Anti-Parallel Arrangement of Methylammonium Ions in Perovskites. *Applied Physics Letters* **2016**, *109*, 213504.

(14) Frost, J. M.; Butler, K. T.; Walsh, A. Molecular Ferroelectric Contributions to Anomalous Hysteresis in Hybrid Perovskite Solar Cells. *APL MATERIALS* **2014**, *2*, 081506.

(15) Zheng, F.; Tan, L. Z.; Liu, S.; Rappe, A. M. Rashba Spin–Orbit Coupling Enhanced Carrier Lifetime in CH3NH3PbI3. *Nano Letters* **2015**, *15*, 7794–7800.

(16) Even, J.; Pedesseau, L.; Katan, C. Comment on "Density Functional Theory Analysis of Structural and Electronic Properties of Orthorhombic Perovskite CH $_3$ NH $_3$ PbI $_3$

520 " by Y. Wang et Al., Phys. Chem. Chem. Phys., 2014, **16** , 1424–1429. *Phys. Chem.*
521 *Chem. Phys.* **2014**, *16*, 8697–8698.

522 (17) Motta, C.; El-Mellouhi, F.; Kais, S.; Tabet, N.; Alharbi, F.; Sanvito, S. Revealing the
523 Role of Organic Cations in Hybrid Halide Perovskite CH3NH3PbI3. *Nature Communi-*
524 *cations* **2015**, *6*, 7026.

525 (18) Etienne, T.; Mosconi, E.; De Angelis, F. Dynamical Origin of the Rashba Effect in
526 Organohalide Lead Perovskites: A Key to Suppressed Carrier Recombination in Per-
527 ovskite Solar Cells? *The Journal of Physical Chemistry Letters* **2016**, *7*, 1638–1645.

528 (19) Rakita, Y.; Bar-Elli, O.; Meirzadeh, E.; Kaslasi, H.; Peleg, Y.; Hodes, G.;
529 Lubomirsky, I.; Oron, D.; Ehre, D.; Cahen, D. Tetragonal CH3NH3PbI3 Is Ferro-
530 electric. *Proceedings of the National Academy of Sciences* **2017**, *114*, E5504–E5512.

531 (20) Fan, Z.; Xiao, J.; Sun, K.; Chen, L.; Hu, Y.; Ouyang, J.; Ong, K. P.; Zeng, K.; Wang, J.
532 Ferroelectricity of $CH_3NH_3PbI_3$ Perovskite. *The Journal of Physical Chemistry*
533 *Letters* **2015**, *6*, 1155–1161.

534 (21) Dastidar, S.; Li, S.; Smolin, S. Y.; Baxter, J. B.; Fafarman, A. T. Slow Electron–Hole
535 Recombination in Lead Iodide Perovskites Does Not Require a Molecular Dipole. *ACS*
536 *Energy Letters* **2017**, *2*, 2239–2244.

537 (22) Yaffe, O.; Guo, Y.; Tan, L. Z.; Egger, D. A.; Hull, T.; Stoumpos, C. C.; Zheng, F.;
538 Heinz, T. F.; Kronik, L.; Kanatzidis, M. G.; Owen, J. S.; Rappe, A. M.; Pimenta, M. A.;
539 Brus, L. E. Local Polar Fluctuations in Lead Halide Perovskite Crystals. *Physical Re-*
540 *view Letters* **2017**, *118*, 136001.

541 (23) Ma, J.; Wang, L.-W. Nanoscale Charge Localization Induced by Random Orientations
542 of Organic Molecules in Hybrid Perovskite $CH_3NH_3PbI_3$. *Nano Letters* **2015**, *15*,
543 248–253.

(24) Ma, J.; Wang, L.-W. The Nature of Electron Mobility in Hybrid Perovskite $CH_3NH_3PbI_3$. *Nano Letters* **2017**, *17*, 3646–3654.

(25) Ambrosio, F.; Wiktor, J.; Angelis, F. D.; Pasquarello, A. Origin of Low Electron–hole Recombination Rate in Metal Halide Perovskites. *Energy & Environmental Science* **2018**, *11*, 101–105.

(26) Kang, J.; Wang, L.-W. Dynamic Disorder and Potential Fluctuation in Two-Dimensional Perovskite. *The Journal of Physical Chemistry Letters* **2017**, *8*, 3875–3880.

(27) Frost, J. M.; Whalley, L. D.; Walsh, A. Slow Cooling of Hot Polarons in Halide Perovskite Solar Cells. *ACS Energy Letters* **2017**, *2*, 2647–2652.

(28) Kawai, H.; Giorgi, G.; Marini, A.; Yamashita, K. The Mechanism of Slow Hot-Hole Cooling in Lead-Iodide Perovskite: First-Principles Calculation on Carrier Lifetime from Electron–Phonon Interaction. *Nano Letters* **2015**, *15*, 3103–3108.

(29) Wright, A. D.; Verdi, C.; Milot, R. L.; Eperon, G. E.; Pérez-Osorio, M. A.; Snaith, H. J.; Giustino, F.; Johnston, M. B.; Herz, L. M. Electron–phonon Coupling in Hybrid Lead Halide Perovskites. *Nature Communications* **2016**, *7*, 11755.

(30) Herz, L. M. Charge-Carrier Mobilities in Metal Halide Perovskites: Fundamental Mechanisms and Limits. *ACS Energy Letters* **2017**, *2*, 1539–1548.

(31) Yu, Z.-G. Rashba Effect and Carrier Mobility in Hybrid Organic–Inorganic Perovskites. *The Journal of Physical Chemistry Letters* **2016**, *7*, 3078–3083.

(32) Zhu, X.-Y.; Podzorov, V. Charge Carriers in Hybrid Organic–Inorganic Lead Halide Perovskites Might Be Protected as Large Polarons. *The Journal of Physical Chemistry Letters* **2015**, *6*, 4758–4761.

(33) Bischak, C. G.; Hetherington, C. L.; Wu, H.; Aloni, S.; Ogletree, D. F.; Limmer, D. T.; Ginsberg, N. S. Origin of Reversible Photoinduced Phase Separation in Hybrid Perovskites. *Nano Letters* **2017**, *17*, 1028–1033.

(34) Ivanovska, T.; Dionigi, C.; Mosconi, E.; De Angelis, F.; Liscio, F.; Morandi, V.; Ruani, G. Long-Lived Photoinduced Polarons in Organohalide Perovskites. *The Journal of Physical Chemistry Letters* **2017**, *8*, 3081–3086.

(35) Neukirch, A. J.; Nie, W.; Blancon, J.-C.; Appavoo, K.; Tsai, H.; Sfeir, M. Y.; Katan, C.; Pedesseau, L.; Even, J.; Crochet, J. J.; Gupta, G.; Mohite, A. D.; Tretiak, S. Polaron Stabilization by Cooperative Lattice Distortion and Cation Rotations in Hybrid Perovskite Materials. *Nano Letters* **2016**, *16*, 3809–3816.

(36) Welch, E.; Scolfaro, L.; Zakhidov, A. Density Functional Theory + U Modeling of Polarons in Organohalide Lead Perovskites. *AIP Advances* **2016**, *6*, 125037.

(37) Nie, W.; Blancon, J.-C.; Neukirch, A. J.; Appavoo, K.; Tsai, H.; Chhowalla, M.; Alam, M. A.; Sfeir, M. Y.; Katan, C.; Even, J.; Tretiak, S.; Crochet, J. J.; Gupta, G.; Mohite, A. D. Light-Activated Photocurrent Degradation and Self-Healing in Perovskite Solar Cells. *Nature Communications* **2016**, *7*, 11574.

(38) FzvNMAN, R. P.; Institute, C. Slow Electrons in a Polar Crystal. 6.

(39) Niesner, D.; Zhu, H.; Miyata, K.; Joshi, P. P.; Evans, T. J. S.; Kudisch, B. J.; Trinh, M. T.; Marks, M.; Zhu, X.-Y. Persistent Energetic Electrons in Methylammonium Lead Iodide Perovskite Thin Films. *Journal of the American Chemical Society* **2016**, *138*, 15717–15726.

(40) Guo, Z.; Wan, Y.; Yang, M.; Snaider, J.; Zhu, K.; Huang, L. Long-Range Hot-Carrier Transport in Hybrid Perovskites Visualized by Ultrafast Microscopy. *Science* **2017**, *356*, 59–62.

(41) Price, M. B.; Butkus, J.; Jellicoe, T. C.; Sadhanala, A.; Briane, A.; Halpert, J. E.; Broch, K.; Hodgkiss, J. M.; Friend, R. H.; Deschler, F. Hot-Carrier Cooling and Photoinduced Refractive Index Changes in Organic–inorganic Lead Halide Perovskites. *Nature Communications* **2015**, *6*, 8420.

(42) Zhu, Z.; Ma, J.; Wang, Z.; Mu, C.; Fan, Z.; Du, L.; Bai, Y.; Fan, L.; Yan, H.; Phillips, D. L.; Yang, S. Efficiency Enhancement of Perovskite Solar Cells through Fast Electron Extraction: The Role of Graphene Quantum Dots. *Journal of the American Chemical Society* **2014**, *136*, 3760–3763.

(43) Yang, J. et al. Acoustic-Optical Phonon up-Conversion and Hot-Phonon Bottleneck in Lead-Halide Perovskites. *Nature Communications* **2017**, *8*, 14120.

(44) Yang, Y.; Ostrowski, D. P.; France, R. M.; Zhu, K.; van de Lagemaat, J.; Luther, J. M.; Beard, M. C. Observation of a Hot-Phonon Bottleneck in Lead-Iodide Perovskites. *Nature Photonics* **2016**, *10*, 53–59.

(45) Miyata, K.; Atallah, T. L.; Zhu, X.-Y. Lead Halide Perovskites: Crystal-Liquid Duality, Phonon Glass Electron Crystals, and Large Polaron Formation. *Science Advances* **2017**, *3*, e1701469.

(46) Miyata, K.; Meggiolaro, D.; Trinh, M. T.; Joshi, P. P.; Mosconi, E.; Jones, S. C.; Angelis, F. D.; Zhu, X.-Y. Large Polarons in Lead Halide Perovskites. *Science Advances* **2017**, *3*, e1701217.

(47) Fröhlich, H. Electrons in Lattice Fields. *Advances in Physics* **1954**, *3*, 325–361.

(48) Jia, W.; Cao, Z.; Wang, L.; Fu, J.; Chi, X.; Gao, W.; Wang, L.-W. The Analysis of a Plane Wave Pseudopotential Density Functional Theory Code on a GPU Machine. *Computer Physics Communications* **2013**, *184*, 9–18.

(49) Jia, W.; Fu, J.; Cao, Z.; Wang, L.; Chi, X.; Gao, W.; Wang, L.-W. Fast Plane Wave Density Functional Theory Molecular Dynamics Calculations on Multi-GPU Machines. *Journal of Computational Physics* **2013**, *251*, 102–115.

(50) Perdew, J. P.; Burke, K.; Ernzerhof, M. Generalized Gradient Approximation Made Simple. *Physical review letters* **1996**, *77*, 3865.

(51) Zheng, F.; Brehm, J. A.; Young, S. M.; Kim, Y.; Rappe, A. M. Substantial Optical Dielectric Enhancement by Volume Compression in LiAsSe 2. *Physical Review B* **2016**, *93*.

(52) Hamann, D. R. Optimized Norm-Conserving Vanderbilt Pseudopotentials. *Physical Review B* **2013**, *88*, 085117.

(53) Giannozzi, P. et al. QUANTUM ESPRESSO: A Modular and Open-Source Software Project for Quantum Simulations of Materials. *Journal of Physics: Condensed Matter* **2009**, *21*, 395502.

(54) Marzari, N.; Mostofi, A. A.; Yates, J. R.; Souza, I.; Vanderbilt, D. Maximally Localized Wannier Functions: Theory and Applications. *Reviews of Modern Physics* **2012**, *84*, 1419–1475.

(55) Zheng, F.; Takenaka, H.; Wang, F.; Koocher, N. Z.; Rappe, A. M. First-Principles Calculation of the Bulk Photovoltaic Effect in CH $_3$ NH $_3$ PbI $_3$ and CH $_3$ NH $_3$ PbI $_{3-x}$ Cl $_X$. *The Journal of Physical Chemistry Letters* **2015**, *6*, 31–37.

(56) Amat, A.; Mosconi, E.; Ronca, E.; Quarti, C.; Umari, P.; Nazeeruddin, M. K.; Grätzel, M.; De Angelis, F. Cation-Induced Band-Gap Tuning in Organohalide Perovskites: Interplay of Spin–Orbit Coupling and Octahedra Tilting. *Nano Letters* **2014**, *14*, 3608–3616.

(57) Kim, M.; Im, J.; Freeman, A. J.; Ihm, J.; Jin, H. Switchable S = 1/2 and J = 1/2 Rashba Bands in Ferroelectric Halide Perovskites. *Proceedings of the National Academy of Sciences* **2014**, *111*, 6900–6904.

(58) Maschho, K. J.; Sorensen, D. C. P ARPACK: An E Cient Portable Large Scale Eigenvalue Package for Distributed Memory Parallel Architectures. *Applied Parallel Computing in Industrial Problems and Optimization, Lecture Notes in Computer Science* **1996**, *1184*.

(59) Yaffe, O.; Guo, Y.; Tan, L. Z.; Egger, D. A.; Hull, T.; Stoumpos, C. C.; Zheng, F.; Heinz, T. F.; Kronik, L.; Kanatzidis, M. G.; Owen, J. S.; Rappe, A. M.; Pimenta, M. A.; Brus, L. E. Local Polar Fluctuations in Lead Halide Perovskite Crystals. *Physical Review Letters* **2017**, *118*, 136001.

(60) Sendner, M.; K. Nayak, P.; A. Egger, D.; Beck, S.; Müller, C.; Epding, B.; Kowalsky, W.; Kronik, L.; J. Snaith, H.; Pucci, A.; Lovrinčić, R. Optical Phonons in Methylammonium Lead Halide Perovskites and Implications for Charge Transport. *Materials Horizons* **2016**, *3*, 613–620.

(61) Kirchartz, T.; Markvart, T.; Rau, U.; Egger, D. A. Impact of Small Phonon Energies on the Charge-Carrier Lifetimes in Metal-Halide Perovskites. *arXiv:1801.02169 [cond-mat]* **2018**,

(62) Frost, J. M. Calculating Polaron Mobility in Halide Perovskites. *Physical Review B* **2017**, *96*.

(63) Pérez-Osorio, M. A.; Milot, R. L.; Filip, M. R.; Patel, J. B.; Herz, L. M.; Johnston, M. B.; Giustino, F. Vibrational Properties of the Organic–Inorganic Halide Perovskite CH3NH3PbI3 from Theory and Experiment: Factor Group Analysis, First-Principles Calculations, and Low-Temperature Infrared Spectra. *The Journal of Physical Chemistry C* **2015**, *119*, 25703–25718.

(64) Muljarov, E. A.; Zimmermann, R. Exciton Dephasing in Quantum Dots Due to LO-Phonon Coupling: An Exactly Solvable Model. *Physical Review Letters* **2007**, *98*.

(65) Verbist, G.; Peeters, F. M.; Devreese, J. T. Extended Stability Region for Large Bipolarons through Interaction with Multiple Phonon Branches. *Ferroelectrics* **1992**, *130*, 27–34.

(66) Zheng, K.; Abdellah, M.; Zhu, Q.; Kong, Q.; Jennings, G.; Kurtz, C. A.; Messing, M. E.; Niu, Y.; Gosztola, D. J.; Al-Marri, M. J.; Zhang, X.; Pullerits, T.; Canton, S. E. Direct Experimental Evidence for Photoinduced Strong-Coupling Polarons in Organolead Halide Perovskite Nanoparticles. *The Journal of Physical Chemistry Letters* **2016**, *7*, 4535–4539.

(67) Devreese, J. T. Frohlich Polarons. Lecture Course Including Detailed Theoretical Derivations. *arXiv preprint arXiv:1611.06122* **2016**,

(68) Plimpton, S. Fast parallel algorithms for short-range molecular dynamics. *Journal of computational physics* **1995**, *117*, 1–19.

(69) Mattoni, A.; Filippetti, A.; Saba, M. I.; Delugas, P. Methylammonium Rotational Dynamics in Lead Halide Perovskite by Classical Molecular Dynamics: The Role of Temperature. *The Journal of Physical Chemistry C* **2015**, *119*, 17421–17428.

(70) Mayers, M. Z.; Tan, L. Z.; Egger, D. A.; Rappe, A. M.; Reichman, D. R. How Lattice and Charge Fluctuations Control Carrier Dynamics in Halide Perovskites. *Nano Letters* **2018**, *18*, 8041–8046.

(71) Milot, R. L.; Eperon, G. E.; Snaith, H. J.; Johnston, M. B.; Herz, L. M. Temperature-Dependent Charge-Carrier Dynamics in CH3NH3PbI3 Perovskite Thin Films. *Advanced Functional Materials* **2015**, *25*, 6218–6227.

(72) Gélvez-Rueda, M. C.; Cao, D. H.; Patwardhan, S.; Renaud, N.; Stoumpos, C. C.; Schatz, G. C.; Hupp, J. T.; Farha, O. K.; Savenije, T. J.; Kanatzidis, M. G.; Grozema, F. C. Effect of Cation Rotation on Charge Dynamics in Hybrid Lead Halide Perovskites. *The Journal of Physical Chemistry C* **2016**, *120*, 16577–16585.

(73) Guo, Z.; Manser, J. S.; Wan, Y.; Kamat, P. V.; Huang, L. Spatial and Temporal Imaging of Long-Range Charge Transport in Perovskite Thin Films by Ultrafast Microscopy. *Nature Communications* **2015**, *6*, 7471.

(74) Oga, H.; Saeki, A.; Ogomi, Y.; Hayase, S.; Seki, S. Improved Understanding of the Electronic and Energetic Landscapes of Perovskite Solar Cells: High Local Charge Carrier Mobility, Reduced Recombination, and Extremely Shallow Traps. *Journal of the American Chemical Society* **2014**, *136*, 13818–13825.

(75) Lim, J.; T. Hörantner, M.; Sakai, N.; M. Ball, J.; Mahesh, S.; K. Noel, N.; Lin, Y.-H.; B. Patel, J.; P. McMeekin, D.; B. Johnston, M.; Wenger, B.; J. Snaith, H. Elucidating the Long-Range Charge Carrier Mobility in Metal Halide Perovskite Thin Films. *Energy & Environmental Science* **2019**, *12*, 169–176.

(76) Wehrenfennig, C.; Eperon, G. E.; Johnston, M. B.; Snaith, H. J.; Herz, L. M. High Charge Carrier Mobilities and Lifetimes in Organolead Trihalide Perovskites. *Advanced Materials* **2014**, *26*, 1584–1589.

(77) Karakus, M.; Jensen, S. A.; D'Angelo, F.; Turchinovich, D.; Bonn, M.; Cánovas, E. Phonon–Electron Scattering Limits Free Charge Mobility in Methylammonium Lead Iodide Perovskites. *The Journal of Physical Chemistry Letters* **2015**, *6*, 4991–4996.

(78) Zhou, J.; Lei, N.; Zhou, H.; Zhang, Y.; Tang, Z.; Jiang, L. Understanding the Temperature-Dependent Charge Transport, Structural Variation and Photoluminescent Properties in Methylammonium Lead Halide Perovskite Single Crystals. *Journal of Materials Chemistry C* **2018**, *6*, 6556–6564.

(79) Shrestha, S.; Matt, G. J.; Osvet, A.; Niesner, D.; Hock, R.; Brabec, C. J. Assessing Temperature Dependence of Drift Mobility in Methylammonium Lead Iodide Perovskite Single Crystals. *The Journal of Physical Chemistry C* **2018**, *122*, 5935–5939.

(80) Tan, L. Z.; Zheng, F.; Rappe, A. M. Intermolecular Interactions in Hybrid Perovskites Understood from a Combined Density Functional Theory and Effective Hamiltonian Approach. *ACS Energy Letters* **2017**, *2*, 937–942.

(81) Li, B.; Kawakita, Y.; Liu, Y.; Wang, M.; Matsuura, M.; Shibata, K.; Ohira-Kawamura, S.; Yamada, T.; Lin, S.; Nakajima, K.; Liu, S. F. Polar Rotor Scattering as Atomic-Level Origin of Low Mobility and Thermal Conductivity of Perovskite CH3NH3PbI3. *Nature Communications* **2017**, *8*, 16086.

(82) Kadanoff, L. P. Boltzmann Equation for Polarons. *Physical Review* **1963**, *130*, 1364–1369.

(83) Christov, S. G. Adiabatic Polaron Theory of Electron Hopping in Crystals: A Reaction-Rate Approach. *Physical Review B* **1982**, *26*, 6918–6935.

34